Nanoscale

PAPER

View Article Online
View Journal | View Issue

Cite this: *Nanoscale*, 2025, **17**, 21640

Aluminum surface lattice resonances for enhanced near-infrared performance in asymmetric environments

Pascal Cheng,[a] Stéphanie Lau-Truong,[a] Sarra Gam-Derouich,[a] Roméo Bonnet,[a] Alexandre Chevillot-Biraud,[a] Macilia Braïk,[b] Abdelaziz Mezeghrane,[b] Abderrahmane Belkhir,[b] Shang Li,[c] Manon Dewynter,[c] Renaud Bachelot,[c,d] Anne-Laure Baudrion[c] and Nordin Félidj *[a]

Aluminum (Al) is a cost-effective alternative to noble metals for plasmonics, particularly in the ultraviolet (UV) and visible regions. However, in the near-infrared (NIR) region, its performance is hindered by interband transitions (IBTs) at around 825 nm, leading to increased optical losses and broad resonances. Surface lattice resonances (SLRs) offer a promising solution by enhancing the plasmonic quality factor (*Q*-factor) through coherent coupling of localized surface plasmon (LSP) modes with Rayleigh anomalies. Although high-*Q* SLRs have been demonstrated in homogeneous environments, achieving similar enhancements in asymmetric media such as air remains a challenge. This study presents a novel approach for improving the *Q* factor of aluminum in air by utilizing SLRs in aluminum nanoparticle (NP) arrays fabricated *via* electron beam lithography (EBL) on a high refractive index indium tin oxide (ITO) substrate. The ITO substrate enhances long-range coupling between NPs, reinforcing coherent interactions. Using absorption micro-spectrometry and finite-difference time-domain (FDTD) simulations, we demonstrate *Q* factors reaching 110 in air, significantly exceeding typical values in IR in an asymmetrical surrounding medium. Our results establish aluminum as a viable low-cost material for high-performance plasmonic applications in sensing, telecommunications, and optoelectronics.

Received 3rd June 2025,
Accepted 12th August 2025

DOI: 10.1039/d5nr02363g

rsc.li/nanoscale

1 Introduction

Metallic nanoparticles (NPs) absorb and scatter light due to their ability to support localized surface plasmon (LSP) resonances.[1–3] These resonances involve coherent oscillations of surface conduction electrons in response to the incident electric field of light, leading to the generation of an enhanced optical near-field.[4–6] The amplification of the local field results from a significant dipole moment at optical frequencies induced by electron oscillations. The LSP frequency of a metallic NP is closely influenced by the particle's size and shape, as well as the permittivity of the metal and the surrounding medium.[7–10]

Aluminum (Al) is frequently used in plasmonics due to its lower cost and higher abundance compared to precious metals such as gold and silver.[11–18] Moreover, at ultraviolet (UV) and near-visible wavelengths, aluminum is more suitable for large-scale applications, such as optical sensors, photovoltaics, and nanoantennas.[19–23] Optimizing the quality factor (*Q* factor), defined as the ratio $\lambda/\Delta\lambda$ (λ is the wavelength of the plasmon and $\Delta\lambda$ is the full width at half maximum of the plasmon resonance), is highly desirable and still remains a challenge for aluminum, especially for applications that require high-sensitivity sensing or strong light–matter interactions.[24–26] Indeed, aluminium nanoparticles show poor *Q*-factors in the visible wavelength range, around 2–4, limiting the latter applications.[12,27] One way to improve the quality factor is to take advantage of the excitation of surface lattice resonances (SLRs).[28–38] These modes arise from coherent coupling of single NP LSP resonance by the in-plane diffraction orders of the lattice, so-called Rayleigh anomalies (RAs). The most relevant feature in the extinction spectra is the emergence of an additional band, with an asymmetric line shape – Fano profile – resulting from the interference between the broad resonance in the individual NPs and the narrow resonance given by the RA.[39,40] Using this approach,

[a]*Université Paris Cité, Laboratoire ITODYS, CNRS, F-75006 Paris, France. E-mail: nordin.felidj@u-paris.fr*
[b]*Université Mouloud Mammeri de Tizi-Ouzou, Laboratoire LPCQ, BP 17 RP 15000 Tizi-Ouzou, Algeria*
[c]*Laboratoire L2n – CNRS UMR 7076, Université de Technologie de Troyes (UTT), European University of Technology Institute of Nanomaterials and Nanotechnologies (EUTINN), European University of Technology, European Union*
[d]*CINTRA CNRS IRL 3288, EEE School, Nanyang Technological University, Singapore*

researchers have demonstrated a reduced line width with higher *Q*-factor SLRs in the UV region. For instance, X. Zhu *et al.*, have shown remarkably high *Q*-factors in water, up to 53, for wavelengths below 500 nm.[27] More recently, B. W. Lin *et al.* provided an in-depth analysis of the properties of SLRs with an experimental *Q*-factor of 125 (in silica) in the UV region using a one-dimensional aluminum grating.[41]

In the near-infrared region, aluminum has limitations because of interband transitions (IBTs) occurring near the visible-to-NIR spectral range, making it less practical compared to metals like silver and gold. Such IBTs occur when electrons in the material are excited from a lower energy band (typically the valence band) to a higher energy band (typically the conduction band), absorbing energy from incident light. The IBT for Al is centered at around 825 nm, leading to higher ohmic losses, degrading the optical performance of aluminum-based plasmonic devices in this spectral range, while it is crucial for various plasmonic applications, including telecommunications (800–1600 nm), NIR sensing, optoelectronic devices, and photovoltaics.[38,42–44] Additionally, it also aligns with the transparency window of most living tissues, making it particularly suitable for non-invasive and non-destructive medical diagnostics and treatments. As a result, the *Q*-factor of the plasmonic resonance is significantly reduced, leading to broader and less well-defined resonances in the NIR spectrum. To enhance the *Q*-factors in the NIR region, recent studies have explored the implementation of SLRs. For instance, L. Li *et al.* proposed bimodal SLR sensors based on asymmetric Al nanoparticles deposited on an Al film, with SLR wavelengths located in the red spectral range.[45] These sensors showed good sensitivity to refractive index changes but exhibited relatively low *Q*-factors (around 30). In a separate study, the same authors reported *Q*-factor values of up to 42 in the visible range using Al NPs.[46] In another work, Bin Alam *et al.* explored the degree of freedom polarization in Al V-shaped NPs arranged in rectangular periodic arrays. Using incident collimated light in normal incidence and a broadband supercontinuum laser source, they achieved a remarkable quality factor of 800 at a wavelength of 1160 nm in a homogeneous surrounding medium, where optimal SLR properties are anticipated.[47]

However, developing SLR-based devices in an inhomogeneous environment presents significant challenges.[48] For example, operating in air or water is crucial for sensing applications but introduces substantial difficulties when employing SLRs. In fact, if symmetrical environments enable optimal coupling of incident light to plasmonic modes, an asymmetrical surrounding medium, in contrast, disrupts phase-matching conditions, thereby diminishing excitation efficiency and propagation. Specifically, asymmetry in the medium introduces a refractive index mismatch, weakening constructive interference between modes.[49] This reduction in interference results in diminished field enhancement and, consequently, lower sensing performance.

The substrate clearly plays a key role in modulating surface lattice resonances (SLRs), near-field coupling, and field enhancement. Dielectric layers or conductive films like indium tin oxide (ITO) can shift or enable SLR modes in specific spectral regions, as evidenced in recent work. Substrate-induced asymmetries also affect dispersion and mode selection, influencing emission directionality and coherence. This makes substrate engineering especially important when integrating molecular gain materials and 2D lattices into metasurfaces.[50–53]

The question of improving the quality factor of aluminum, particularly in air for nano-optics applications, has not been explored in the spectral region of interband transition, well known for significantly damping the optical properties of plasmonic particles. This is the primary focus of this article. To overcome this limitation, we propose the fabrication of regularly arranged aluminum nanoparticles (made by electron beam lithography, EBL) sustaining SLR modes. In order to improve SLR efficiency, the NPs are deposited on a high-refractive-index indium tin oxide substrate. Indeed, the high refractive index of the ITO substrate can act as an efficient waveguide, enhancing long-range coupling between the NPs. We experimentally and theoretically investigate the optical response of circular aluminum disk arrays in air using a visible–NIR absorption micro-spectrometer and analyze the impact of different interparticle distances (grating constants) and diameters on the *Q*-factors. Theoretical calculations were performed using the finite-difference time-domain (FDTD) method. We show that these *Q*-factors are further amplified by the efficient coherent coupling between particles facilitated by guided modes in the ITO substrate, with a remarkable increase in the IBT region compared to values found in the ultraviolet (UV) region, despite the limitations inherent to this spectral region. Experimental *Q*-factor values reach up to 110 in air, highlighting the potential of aluminum, a cheap and abundant metal, for advanced device applications in the NIR region.

2 Results and discussion

The optical performance of aluminum NPs gradually decreases beyond the UV spectral range. This decline is primarily attributed to the increase in the imaginary part of aluminum's dielectric function with increasing wavelength, as shown in Fig. 1. The figure illustrates the real and imaginary components of the dielectric function (ε) of aluminum *versus* wavelength (in nm) and energy (in eV) extracted from the experimental data of Rakić *et al.*[54] These are in good agreement with the data from the Drude–Lorentz model, with plots derived from the formula given in the SI (eqn (S1)–(S3)). While the real part of ε determines the wavelength of the plasmon resonance, the imaginary part quantifies the damping of the optical performance of plasmonic structures. As evidenced in Fig. 1a, the imaginary part of (ε) indicates stronger damping in the NIR region.

This damping originates from two primary factors: (i) *interband transitions (IBTs).* For aluminum, they arise from electronic transitions between electronic discrete energy levels. IBTs can be described using the Lorentz model (see Fig. 1b and eqn (S2) in

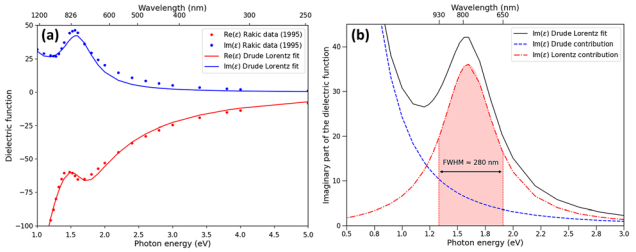

Fig. 1 (a) Complex dielectric function of aluminum as a function of wavelength and energy, with experimental data from the work of Rakić *et al.*, represented by red and blue dots for the real and imaginary components, respectively. Theoretical calculations based on the Drude–Lorentz model are shown as solid red and blue lines for the real and imaginary components, respectively. (b) Imaginary part of the dielectric constant of aluminum plotted using the Drude–Lorentz model (solid dark line). The Drude (blue dots) and Lorentz (red dashed line) contributions to the above model are plotted separately.

the SI). As shown in Fig. 1b, the Lorentz contribution produces a peak in the imaginary part of the dielectric function centered at approximately 1.5 eV or 825 nm (red dashed line), with a full width at half maximum (FWHM) of 0.7 eV (280 nm); (ii) *bulk aluminum damping*. For higher wavelengths, this damping becomes even more significant, as displayed in Fig. 1b (blue dashed line). This behavior is modeled using the Drude model (eqn (S3) in the SI), showing that Im(ε) increases with increasing wavelength. The combined effects significantly reduce the optical efficiency of aluminum nanoparticles, limiting their applicability in the NIR region. For example, Fig. S1(a–c) illustrates the calculated extinction spectrum in air, obtained through the FDTD method, for a single disk with a diameter varying from 135 to 240 nm (height: 60 nm) deposited on an 80 nm thick ITO layer. The results clearly show a strong damping of the LSP band in the NIR region.

To overcome this limitation, we aim to take advantage of the long-range interactions between aluminum nanoparticles to generate SLRs on a high-refractive-index ITO layer, which acts as a waveguide. Indeed, beyond facilitating electron evacuation during the electron beam lithography process, the ITO layer can function as a waveguide, potentially enhancing long-range interactions between particles. The excitation of SLRs originates from the diffraction of photonic modes in the substrate. These modes emerge only when the particles are separated by specific distances, defined by the grating constant Λ.[55] For example, in a square array, the first-order mode associated with a grazing wave – referred to as the Rayleigh anomaly in the plane – occurs when $\Lambda = \lambda/n$, where λ is the incident wavelength and n is the refractive index of the substrate. This long-range coupling mechanism introduces an additional peak in the extinction spectrum, distinct from the LSP resonance. This SLR peak exhibits a higher quality factor (Q-factor) compared to the LSP resonance, reflecting its enhanced coherence.

In this work, we focus on the square arrays of circular Al disks with diameters (D) ranging from 100 to 240 nm and a fixed height (H = 60 nm). The grating constants (Λ) vary from 292 nm to 679 nm experimentally (measured by scanning electron microscopy). These NPs are deposited on a thin layer of indium tin oxide with a thickness of 80 nm, deposited on a glass substrate. A schematic representation and a SEM image of the fabricated device are provided in the SI (Fig. S2a and S2b). As mentioned previously, the ITO layer can act as a waveguide. This effect occurs if its refractive index exceeds those of both the superstrate (air, in our case) and the glass substrate (with a refractive index of 1.52). Ellipsometry measurements performed on the provided ITO layers, as shown in Fig. S3, indicate that the refractive index is complex but has a very small imaginary part. The experimental data align closely with the values reported by Minenkov *et al.*,[56] showing a decrease in the refractive index with increasing wavelength, reaching values close to 1 in the NIR. Interestingly, annealing the ITO substrate at 500 °C leads to a significant increase in its refractive index, as evidenced by the ellipsometric measurements. Thermal annealing significantly alters the structural and optical properties of ITO thin films by facilitating oxygen absorption from the air into the ITO layer. This process reduces oxygen vacancies and defect densities, thereby enhancing the material's optical and electronic properties.[57,58] This is particularly the case in the NIR range, as shown in Fig. SI.3. For example, at λ = 1000 nm, the refractive index of the annealed sample nearly doubles, reaching approximately 2, compared to a refractive index of 1.25 for the non-annealed ITO sample. Given these values, as well as those of the superstrate and the glass beneath the ITO, the latter can potentially act as a waveguide.

The key question is: combined with SLR excitation, to what extent does the increase in the refractive index of the ITO layer improve the optical properties of the Al NPs in the NIR region? To address this, we first conducted a set of experiments comparing the optical responses of two distinct Al NP arrays before and after annealing the ITO layer. Each array was composed of particles with a diameter D = 135 nm and a height H = 60 nm, but with grating constants Λ = 292 nm and Λ = 489 nm (reflecting the exact values obtained from the SEM measurements). The lowest grating constant Λ = 292 nm has been chosen such that there is no (or very little) far-field coherent coupling between the nanoparticles, while Λ = 489 nm is such that there is a coherent interaction leading to the emergence of an SLR mode. Finite-Difference Time-Domain (FDTD) simulations were conducted using the same geometric parameters as in the experimental setup. The refractive index of indium tin oxide was incorporated based on ellipsometry measurements, considering both non-annealed and annealed conditions. To account for the spontaneous formation of an alumina passivation layer over time, a 5 nm-thick aluminum oxide shell was incorporated around the nanoparticles.[14,15] Note that the Al_2O_3 capping layer effectively passivates the structure, preserving SLR quality over time without impacting the optical response, as confirmed by unchanged extinction spectra six months post-fabrication.

Fig. 2 displays the experimental (black curves) and FDTD-calculated (red curves) extinction spectra of the two arrays,

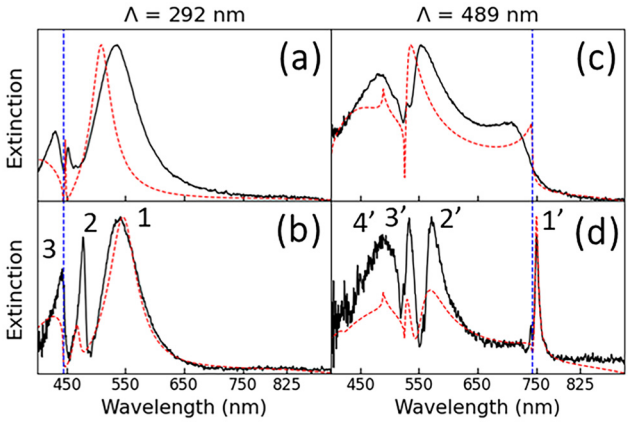

Fig. 2 Extinction spectra in air for the square arrays of aluminum disks (D = 135 nm and H = 60 nm): (a) experimental data (black line) and FDTD simulation (red dashed line) for a non-annealed sample with a grating constant Λ = 292 nm; (b) experimental data (black line) and FDTD simulation (red dashed line) for an annealed sample with a grating constant Λ = 292 nm; (c) experimental data (black line) and FDTD simulation (red dashed line) for a non-annealed sample with a grating constant Λ = 489 nm; and (d) experimental data (black line) and FDTD simulation (red dashed line) for an annealed sample with a grating constant Λ = 489 nm. The vertical blue dashed line indicates the wavelength of the Rayleigh anomaly of order (0, ±1).

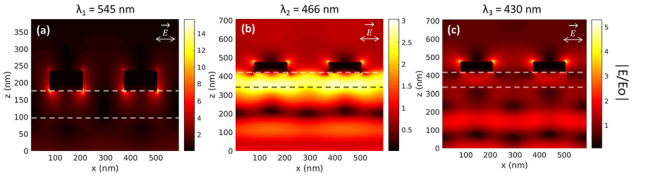

Fig. 3 FDTD simulation results depicting the XZ mapping of the modulus of the normalized electric field for an annealed square array of aluminum nanoparticles with diameter D = 135 nm, height H = 60 nm, and grating constant Λ = 292 nm: (a) at 545 nm, (b) at 466 nm, and (c) at 430 nm, corresponding respectively to spectral peaks 1, 2 and 3 observed in Fig. 2b. The dashed lines represent the ITO waveguide layer.

both before and after annealing the ITO substrate. We first examine the extinction spectra for Λ = 292 nm (Fig. 2a) before annealing the ITO substrate. In the calculated spectrum, a prominent band appears at 508 nm in the extinction spectrum, attributed to the dipolar plasmon mode. This grating constant is such that a limited long-range coupling takes place. This is evident as the first-order (0, ±1) Rayleigh anomaly (marked as blue dashed vertical lines at a minimum of extinction) occurs at 444 nm (far from 508 nm). The experimental spectrum aligns well qualitatively with the FDTD-calculated spectrum, with a slightly larger experimental FWHM attributed to minor polydispersity in the diameter of the nanostructures. Interestingly, two additional peaks, less intense, and two minima are observed at shorter wavelengths (447 nm and 409 nm). After annealing, the dipolar mode (referred to as peak 1 in Fig. 2b) exhibits a slight red shift, located at 545 nm, as confirmed by the FDTD-calculated spectrum. This is attributed to the increased refractive index of ITO, as evidenced in Fig. S3. The two shorter-wavelength peaks at 466 nm and 430 nm (denoted as peaks 2 and 3, respectively) become more pronounced and intense, exhibiting a slight red shift compared to the non-annealed sample. The extinction spectra of the annealed sample show remarkable agreement between experimental measurements and FDTD simulations. This alignment is mainly due to the consideration of the true values of the optical index of annealed ITO in the simulations. Note that the refractive index of aluminum remained unchanged before and after annealing.

To confirm the origin of peak 1, the distribution of electric field, along the XZ plane intercepting the nanoparticles, was plotted using FDTD (see Fig. 3a). FDTD calculations were also performed along the X and Y axes at the air/ITO interface (corresponding to a height of H = 0 nm; see Fig. S4a) and at H = 60 nm (corresponding to the height of the NPs; see Fig. S4d). Peak 1, located at 545 nm, is clearly associated with a dipolar LSP mode (Fig. 3a). Indeed, the lobes of the dipolar resonance are observable in the cross-section and characterized by two maxima in the electric field emerging symmetrically from the nanoparticle surface along the direction of the incident polarization (Fig. S4a and S4d). Therefore, as shown in Fig. 3a, the electric field maxima are clearly located near the regions of high refractive index.

To investigate the origin of peaks 2 and 3, the distribution of the electric field was plotted along the X and Z axes, (see Fig. 3b and c) and along the X and Y axes (Fig. S4b–S4f). At 466 nm (peak 2); the XZ mapping (Fig. 3b) clearly reveals the excitation of a guided mode (GM) whose position is just above the (0, ±1) anomaly. This peak arises from the combined contributions of the lattice mode ((0, ±1) anomaly), the guided mode in the ITO layer, and the LSP resonance of the metallic particles. The distribution of the electric field modulus, calculated just below the particles, shows four lobes (Fig. S4b), unlike the one calculated in the superstrate at H = 60 nm (Fig. S4e), which only shows two lobes. This confirms that this resonance is basically dipolar. On the substrate side, due to its interaction with the GM excited in the ITO layer, the GM, which propagates along the (O_y) axis, interferes with the localized plasmonic mode, leading to the appearance of dark fringes in the particles, causing the two lobes to split. The E-maps calculated in the XY planes intersecting the particles (Fig. S4) show that as one moves away from the ITO layer (and the GM), the lobes, initially separated by the effect of the GM mode, come closer together, and the resonance regains its dipolar character. Similar results have been reported by R. Guo *et al.*, who studied the optical response of gold disk arrays deposited on a thin alumina layer, itself supported by a quartz substrate.[59] In their study, a similar peak was observed on the blue side of the dipolar mode, attributed to the excitation of a quadrupolar mode. This phenomenon was related to the higher refractive index (RI = 1.76) of the alumina intermediate layer compared to the superstrate (water, RI = 1.33) and the substrate (quartz, RI = 1.45), thus acting as a waveguide.

Because of the higher refractive index, total internal reflection occurred within the alumina layer when the incident angle equaled or exceeded the critical angle. As a result, reflections occur at both interfaces. The reflected light interacts with nearby nanoparticles, supporting both vertical and horizontal components of the electric field, thereby exciting the quadrupolar mode in the nanoparticles. In our case, for the annealed sample, where the ITO intermediate layer acts as a waveguide, peak 2 can be identified as a quadrupolar mode, driven by the presence of both vertical and horizontal components of the electric field due to total internal refection in the ITO waveguide. Notably, while a clear quadrupolar behavior is observed at H = 0 nm (at the ITO/air interface, Fig. S4b), the mapping reveals a dipolar profile at H = 60 nm (corresponding to the height at the top of the NPs), as evidenced in Fig. S4e. This means that two modes – dipolar and quadrupolar – coexist within the same NP, as shown in the electric field mapping at H = 0 nm and H = 60 nm. Such an effect has been observed and explained in detail by A. Muravitskaya *et al.* and attributed to an asymmetrical surrounding medium.[60] Note that for the non-annealed sample, where the low refractive index of the ITO layer prevents the formation of waveguide modes, both the experimental and calculated spectra exhibit a much less pronounced quadrupolar mode. This reduction is likely due to the absence or near-absence of reflected light in the ITO layer.

In contrast to peak 2, the field mapping at 430 nm, corresponding to the wavelength of peak 3, reveals another plasmon mode with a dipolar character (Fig. 3c, Fig. S4c and S4f). This broad resonance corresponds to a LSP without any significant coupling with the Rayleigh anomaly, as can be seen in these last figures.

In Fig. 2c and d, we focus on a grating constant, Λ = 489 nm, corresponding to a strong coherent coupling between particles. This grating constant is designed to generate a (0, ±1) diffracted order positioned at approximately 734 nm. Before the annealing process, the experimental extinction spectrum displays four bands (see Fig. 2c), which qualitatively align with the FDTD-calculated spectrum. No clear evidence of the SLR mode is observed, as the Rayleigh anomaly occurs at a wavelength longer than the LSP resonance, thereby restricting long-range coupling. After annealing, the four distinct bands become significantly more resolved (Fig. 2d). The peak (referred to as peak 1′) located at 750 nm emerges with an extreme sharpness and high quality factor, on the order of Q = 110. This peak is associated with the emergence of a SLR mode, as evidenced in Fig. S5a and S5d. Remarkably, although it is located in the spectral region of the electronic transition band, the quality factor of such a plasmonic mode is the highest observed in the literature for aluminum in an inhomogeneous medium (in air, in our study). The high-quality factor observed in the IBT region could be attributed to a weak coupling between the SLR mode and the IBT, which leads to a Fano-type resonance profile. However, the maximum Q-factor for NPs with different diameters depends mainly on the position of the plasmon wavelength relative to the RA position (as discussed below, see Fig. 7). These maxima are therefore observed well beyond the IBT for NPs with larger diameters, excluding any contribution from a weak coupling between the IBT and the SLR mode. A more detailed explanation is provided in the SI. The enhancement in the quality factor after annealing the ITO is attributed to a red shift in the region of strong coupling between the LSP resonance and the Rayleigh anomaly, resulting from an increase in the ITO refractive index. This ITO layer acts as a waveguide, supporting multiple total internal reflections that strengthen the coupling and consequently improve the quality factor. Finally, three additional bands at 566 nm (denoted 2′), 529 nm (denoted 3′), and 480 nm (denoted 4′) are clearly observed in the calculated extinction spectrum, showing excellent agreement with the experimental one (see Fig. 2d).

To confirm or determine the origin of these peaks, we performed 2D electric field mapping along the X and Z axes (as described in Fig. 4) and along the X and Y axes (as described in Fig. S4). The field map, associated with the sharp resonance at 750 nm (peak 1′), reveals the simultaneous excitation of NP plasmon excitation along the polarization direction and the formation of a standing grazing wave (Rayleigh anomaly) in the perpendicular direction, as shown in Fig. S5a and S5d. This clearly identifies the peak as being attributed to an SLR excitation, resulting from the excitation of a (0, ±1) diffracted order (Fig. 4a). Furthermore, the calculated normalized electric field intensity reaches a maximum value of approximately $I = |E|^2 = 2 \times 10^3$, which is exceptional for this metal in the NIR spectral region. In contrast, the study by O. Lecarme *et al.* observed a Rabi splitting in the optical spectrum at around 825 nm, which resulted in a significant reduction in electric field intensity.[42]

The electric field mapping at 566 nm (peak 2′) corresponds to an LSP mode coupled to the (±1, ±1) RA, as indicated by the field lines oriented at 45° (Fig. 4b, Fig. S5b and S5e). The peak at λ = 528 nm corresponds to an SLR resonance, resulting from the coupling between the LSP resonance and the (±1, ±1) anomaly in the substrate (Fig. 4b). These diagonal wavefronts are particularly highlighted by the mapping of the electric field calculated in the substrate at the minimum of the peak at λ = 529 nm (Fig. S5c and S5e). As shown in the XZ cross-section, the GM mode is not excited in this case due to the shift of the (0, ±1) evanescent order toward longer wavelengths

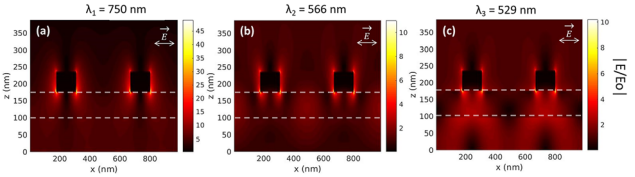

Fig. 4 FDTD simulation results depicting the XZ mapping of the modulus of the normalized electric field for an annealed square array of aluminum nanoparticles with diameter D = 135 nm, height H = 60 nm, and grating constant Λ = 489 nm: (a) at 750 nm, (b) at 566 nm, and (c) at 529 nm, corresponding respectively to spectral peaks 1′, 2′ and 3′ observed in Fig. 2d. The dashed lines represent the ITO waveguide layer.

(greater than 740 nm), preventing its excitation (Fig. 4c). Indeed, these GM modes are efficiently excited only when the structure is sub-wavelength, meaning that it is positioned above the (0, ±1) anomalies. Finally, the peak at λ = 488 nm corresponds to an SLR resonance, resulting from the coupling between the LSP resonance and the (0, ±1) anomaly induced by the superstrate (air).

To highlight the sensitivity of the SLR peak wavelength to the grating constant, we varied the grating constant from Λ = 345 nm to Λ = 627 nm. Fig. 5a and b show the experimental and calculated extinction spectra (for the annealed samples), respectively, with excellent qualitative agreement between the two. As the grating constant increases, the SLR peak corresponding to the Rayleigh anomaly of order (0, ±1), located at the longest wavelengths in the spectrum, undergoes a clear red shift and becomes notably sharper near the IBT region. A high experimental Q-factor of 67 in air is achieved for Λ = 527 nm, corresponding to a resonance at 821 nm, precisely at the center of the interband transition. Interestingly, this grating period is aligned with minimal detuning $\delta = \lambda_{SLR} - \lambda_{RA}$ (Fig. 5b).

As mentioned before, higher-order SLR modes can also be excited. As the grating constant increases, this peak red shifts and becomes sharper, indicating a stronger coupling with the Rayleigh anomaly of the (±1, ±1) order. For example, at Λ = 627 nm, a sharp peak at 697 nm corresponds to an SLR mode coupled with a diffracted order (±1, ±1). This peak exhibits a characteristic Fano-type profile, typical of an SLR mode in phase with the diffracted mode, and its quality factor reaches 64 experimentally. The ability to excite higher-order SLR modes with high Q-factors offers a significant and additional advantage in controlling and enhancing the coupling between SLR modes and diffracted orders in the visible and NIR spectral regions.

Fig. 5c and d display the experimental and calculated dispersion diagrams, respectively. These diagrams show excellent agreement and highlight that as the grating constant increases, the SLR wavelengths associated with the diffracted orders (0, ±1) and (±1, ±1), which approach the Rayleigh anomalies (indicated by the dashed lines), exhibit a reduction in the FWHM, resulting in a higher quality factor. To highlight the importance of ITO annealing on the optical response of the gratings, we compared the experimental and calculated spectra for both the non-annealed and annealed cases at various grating constants (Fig. S6 and S7, respectively). The experimental spectra are in excellent agreement with the calculated ones. Comparison of the spectra obtained before (Fig. S6) and after annealing (Fig. S7) clearly reveals a significant improvement in the optical properties of ITO, particularly in terms of spectral resolution and a reduction in the FWHM. Finally, in order to clearly illustrate the ITO layer's waveguiding role in supporting SLRs, we also performed FDTD simulations for arrays with grating constants Λ = 300 nm and Λ = 500 nm, comparing the extinction spectra with and without an 80 nm ITO layer on glass (Fig. S8). A clear SLR appears only at Λ = 500 nm with the ITO layer, confirming its crucial role in enabling near-infrared SLR modes, as discussed in the SI.

To extract the Q-factor values, we first estimate the FWHM of the different arrays before and after the annealing process (see Fig. 6a and c). The plots show the relationship between the FWHM values and the SLR peaks for each grating constant. Before annealing, the minimum experimental FWHM values are on the order of 40, whereas after annealing, they decrease to less than 10. Consequently, the experimental Q-factor values for the annealed samples are significantly higher, reaching a maximum of 110 (Fig. 6d), compared to 20 for the non-annealed samples (Fig. 6b). Notably, while the experimental data agree well in terms of the SLR wavelengths for the minimum FWHM, the calculated Q-factors are generally higher than the experimental ones, reaching up to 500 for the annealed arrays (Fig. 6d). This discrepancy can be attributed to the fact that our samples are not ideal, unlike the targets used in the FDTD calculations, due to the polydispersity in diameter and surface roughness within the array. More importantly, we achieved the highest Q-factor in air in the most critical spectral region, the IBT region.

As mentioned earlier, while the grating constant plays a crucial role in modulating the wavelength of the SLR mode in the near-infrared region, particularly around the interband transition of aluminum, another approach is to adjust the particle diameter. Indeed, modifying this parameter allows tuning of the SLR wavelength corresponding to the maximum quality factor, thereby providing better control over optical performance across an extended spectral range around the inter-band transition. Therefore, Fig. 7 illustrates the evolution of the quality factor, calculated using the FDTD method, as a function of the SLR wavelength for a given particle diameter. Each

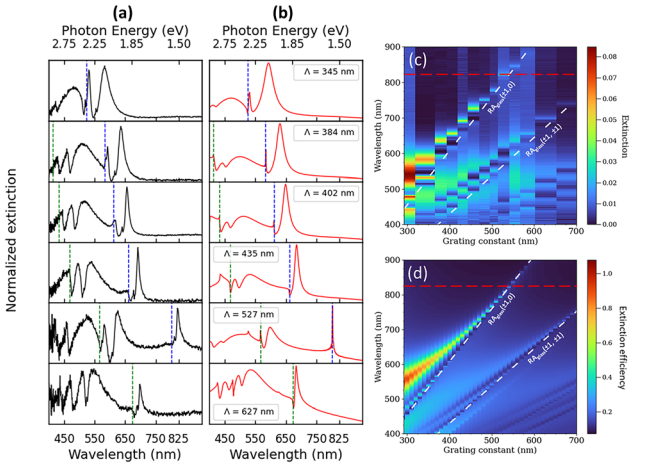

Fig. 5 Comparison between the experimental (a) and FDTD-calculated (b) extinction spectra of annealed Al NP arrays with varying grating constants, Λ, ranging from 345 nm to 627 nm. The vertical blue dashed line indicates the wavelength of the Rayleigh anomaly of order (0, ±1) in the substrate plane, while the vertical green dashed line represents the Rayleigh anomaly of order (±1, ±1). Panels (c) and (d) show the dispersion diagrams corresponding to the experimental and calculated spectra, respectively.

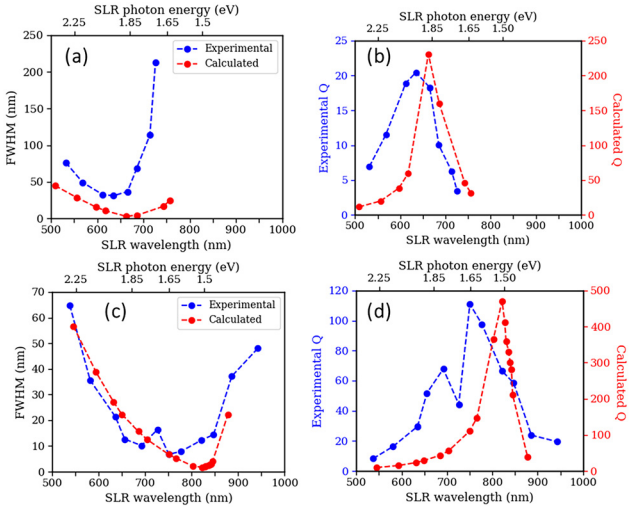

Fig. 6 (a) Experimental (blue dots) and calculated (red dots) values of the full width at half maximum (FWHM) as a function of the SLR modes (associated with the Rayleigh anomaly of order (0, ±1)), corresponding to the non-annealed arrays of Al NPs with grating constants ranging from 292 nm to 679 nm. (b) Experimentally deduced (blue dots) and calculated (red dots) *Q*-factors as a function of the SLR modes. (c) Experimental (blue dots) and calculated (red dots) values of the full width at half maximum (FWHM) as a function of the SLR modes, corresponding to the annealed arrays of Al NPs with grating constants ranging from 292 nm to 679 nm. (d) Experimentally deduced (blue dots) and calculated (red dots) *Q*-factors as a function of the SLR modes.

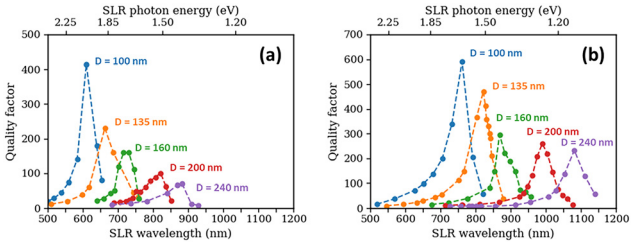

Fig. 7 (a) Calculated *Q*-factor values as a function of the SLR modes for various diameters (ranging from D = 100 nm to D = 240 nm) in a non-annealed array of Al NPs with different grating constant ranges starting from 300 nm to 750 nm. (b) Calculated *Q*-factor values as a function of the SLR modes for the same range of diameters (D = 100 nm to D = 240 nm) in an annealed array of Al NPs, with different grating constant ranges starting from 300 nm to 750 nm. The grating constant ranges were chosen as a function to cover the optimized quality factor of the SLR for each nanoparticle diameter.

SLR wavelength corresponds to the grating constant 400 nm ≤ Λ ≤ 750 nm, as shown in Fig. S9, for NPs with a diameter of D = 240 nm. Fig. 7a and b compare these quality factors before and after ITO annealing. We observe that, at a constant diameter, the maxima of the quality factors are systematically redshifted, exceeding 1100 nm in wavelength, with values reaching approximately 200 for a diameter of D = 240 nm (Fig. 7b). The SLR wavelengths exhibit a significant red shift after the annealing process, as shown in Fig. S10, which compares the dispersion diagrams of the arrays before and after annealing for various NP diameters. This shift is explained by a significant increase in the refractive index of ITO induced by annealing. Furthermore, regardless of the diameters considered, the quality factors are systematically higher after the annealing of ITO. This improvement is attributed to the presence of the waveguide layer, which facilitates the emergence of SLR modes with sharper resonances, in an asymmetrical environment. Note that the maximum *Q*-factors decrease with increasing NP diameter. This can be attributed to the monotonic increase in the imaginary part of the aluminum dielectric constant in the NIR region, as well as retardation effects that become more pronounced in the NPs at larger diameters.[61] However, these last results highlight the importance of simultaneously controlling the grating constant and particle diameter to fully exploit the properties of SLR modes around the interband transition and, more generally, in the near-infrared region.

3 Conclusion

In conclusion, this study highlights the potential of aluminum nanoparticles arranged in regular arrays on high refractive index ITO substrates to significantly enhance quality factors in the interband transition region within an inhomogeneous medium. Through the excitation of surface lattice resonances, the coherent coupling of individual NPs is enhanced by multiple total reflections in the annealed ITO waveguide layer, overcoming the challenges posed by IBT that typically degrade aluminum's optical performance in this spectral range and more generally in the near-infrared region. The experimental results reveal *Q*-factor values as high as 110 in air for Al NPs, even within the IBT region, emphasizing the viability of aluminum as a cost-effective and abundant alternative for advanced plasmonic and nano-optics applications, including sensing and telecommunications.

4 Experimental section

4.1 Experimental

4.1.1 Electron beam lithography. The arrays were fabricated using electron beam lithography (EBL) and characterized by scanning electron microscopy (SEM) using a Zeiss Supra 40 MEB-FEG instrument. To prepare nanostructured surfaces, a 100 nm thick layer of PMMA resist (poly(methyl methacrylate)) was spin-coated onto glass substrates pre-coated with an 80 nm indium tin oxide layer.[62] The nanostructures were defined through electron beam exposure, followed by chemical development. Aluminum was subsequently deposited by thermal evaporation and the process was finalized with a lift-off step, resulting in aluminum nanodisks with a height of 60 ± 5 nm and a diameter of 100 nm. This fabrication method offers precise control over nanoparticle size, shape, and spacing, enabling the fine-tuning of plasmonic resonances at specific wavelengths.[62,63]

4.1.2 Ellipsometric spectrometry. Measurements were performed using a UVISEL–HJY ellipsometric spectrometer. For this study, we performed multiple-wavelength analysis in the 1.5–6 eV range at a fixed incident angle of 70°. The modulator–analyzer configuration was set at M = 0° and A = 45° and did not show discontinuities in determining the ellipsometric angles. To improve analysis, the metallic layers were deposited on polished Si/SiO_2 wafers, previously characterized to reduce the amount of unknown variables in the model. The measures were analyzed through a Drude–Lorentz model, with the simulations directly based on the IS and IC ellipsometric intensities. This allowed reduction of uncertainties due to multiple transformations of the measured signal.

4.1.3 Extinction micro-spectroscopy spectra. The optical response of the samples was analyzed in air using far-field visible–NIR extinction micro-spectroscopy in the wavelength range of 400–1000 nm. Illumination was provided by a halogen lamp from the glass side at normal incidence. The spectrometer (LOT ORIEL model MS 260i) was coupled to an optical microscope (OLYMPUS BX 51) equipped with a 10× objective lens (numerical aperture (N.A.): 0.25). The probed area was a circular spot with a diameter of approximately 125 μm to fit a structured array size of 80 × 80 μm^2.

4.1.4 FDTD calculations. Finite-Difference Time-Domain (FDTD) simulations were performed using Lumerical software. The structure was illuminated at normal incidence from the substrate side with a plane wave on the z axis. In the near field, the normalized electric field intensity was calculated in the vicinity of the aluminum disks at H = 0 nm. For far-field simulations of the extinction spectra, the detector was placed at a distance away from the structure. A perfectly matched layer (PML) was applied along the top and bottom of the z-axis, while periodic boundary conditions were implemented along the x- and y-axes to simulate the nanoparticle arrays. A 5 nm layer of aluminum oxide was added all around the aluminum nanoparticle deposited on a layer of glass coated with 80 nm ITO. A mesh step size of 5 nm was used for the different simulations. To measure the extinction efficiency, we placed a monitor inside the PML region at the top of the arrays to collect the transmitted light T. The extinction efficiency is directly related to T with the following relationship:

$$\mathrm{Ext}_{\mathrm{efficiency}} = -\log 10(T). \quad (1)$$

We used Palik's Handbook of Optical Constants of Solids directly integrated in Lumerical to simulate the refractive indices of aluminum and aluminum oxide. For ITO, we used the results we obtained in ellipsometry for annealed and non-annealed refractive indices. For glass, the refractive index of soda lime glass (n = 1.52) was used.

Conflicts of interest

There are no conflicts to declare.

Data availability

Data for this article, including SEM images, UV-vis measurements and raw data from FDTD calculations are available upon request. See DOI: **https://doi.org/10.1039/d5nr02363g**.

Acknowledgements

This work was supported by grant ANR ADVANSPEC. The project was also partly carried out within the framework of the Graduate School (École Universitaire de Recherche) "NANO-PHOT" (Grant No. ANR-18-EURE-0013).

References

1 K. M. Mayer and J. H. Hafner, *Chem. Rev.*, 2011, **111**, 3828–3857.
2 K. A. Willets and R. P. Van Duyne, *Annu. Rev. Phys. Chem.*, 2007, **58**, 267–297.
3 Y. Chen and H. Ming, *Photonic Sens.*, 2012, **2**, 37–49.
4 C. Girard and A. Dereux, *Rep. Prog. Phys.*, 1996, **59**, 657.
5 D. W. Pohl and D. Courjon, *Near field optics*, Springer Science & Business Media, 2012, vol. 242.
6 A. G. Nikitin, A. V. Kabashin and H. Dallaporta, *Opt. Express*, 2012, **20**, 27941–27952.
7 K. L. Kelly, E. Coronado, L. L. Zhao and G. C. Schatz, *The optical properties of metal nanoparticles: the influence of size, shape, and dielectric environment*, 2003.
8 T. R. Jensen, M. L. Duval, K. L. Kelly, A. A. Lazarides, G. C. Schatz and R. P. Van Duyne, *J. Phys. Chem. B*, 1999, **103**, 9846–9853.
9 M. M. Miller and A. A. Lazarides, *J. Phys. Chem. B*, 2005, **109**, 21556–21565.
10 N. Félidj, J. Grand, G. Laurent, J. Aubard, G. Levi, A. Hohenau, N. Galler, F. Aussenegg and J. Krenn, *J. Chem. Phys.*, 2008, **128**, 094702.
11 D. Gérard and S. K. Gray, *J. Phys. D: Appl. Phys.*, 2014, **48**, 184001.
12 J. Martin, M. Kociak, Z. Mahfoud, J. Proust, D. Gérard and J. Plain, *Nano Lett.*, 2014, **14**, 5517–5523.
13 Y. Ekinci, H. Solak and J. F. Löffler, *J. Appl. Phys.*, 2008, **104**, 083107.
14 C. Langhammer, M. Schwind, B. Kasemo and I. Zoric, *Nano Lett.*, 2008, **8**, 1461–1471.
15 M. W. Knight, N. S. King, L. Liu, H. O. Everitt, P. Nordlander and N. J. Halas, *ACS Nano*, 2014, **8**, 834–840.
16 R. Gillibert, F. Colas, R. Yasukuni, G. Picardi and M. L. de la Chapelle, *J. Phys. Chem. C*, 2017, **121**, 2402–2409.
17 S. Deng, R. Li, J.-E. Park, J. Guan, P. Choo, J. Hu, P. J. Smeets and T. W. Odom, *Proc. Natl. Acad. Sci. U. S. A.*, 2020, **117**, 23380–23384.
18 R. H. Siddique, S. Kumar, V. Narasimhan, H. Kwon and H. Choo, *ACS Nano*, 2019, **13**, 13775–13783.

19 S. J. Tan, L. Zhang, D. Zhu, X. M. Goh, Y. M. Wang, K. Kumar, C.-W. Qiu and J. K. Yang, *Nano Lett.*, 2014, **14**, 4023–4029.
20 M. L. Tseng, J. Yang, M. Semmlinger, C. Zhang, P. Nordlander and N. J. Halas, *Nano Lett.*, 2017, **17**, 6034–6039.
21 M. Takeda, R. Takahara and N. Hasuike, *Opt. Rev.*, 2020, **27**, 427–431.
22 I. Abid, W. Safar, M. Edely, N. Felidj, M. Lamy de la Chapelle and H. Shen, *J. Phys. Chem. C*, 2022, **126**, 8676–8683.
23 J. Guan, R. Li, X. G. Juarez, A. D. Sample, Y. Wang, G. C. Schatz and T. W. Odom, *Adv. Mater.*, 2023, **35**, 2103262.
24 K. Guo, G. Lozano, M. A. Verschuuren and J. Gómez Rivas, *J. Appl. Phys.*, 2015, **118**, 073103.
25 A. Yang, A. J. Hryn, M. R. Bourgeois, W.-K. Lee, J. Hu, G. C. Schatz and T. W. Odom, *Proc. Natl. Acad. Sci. U. S. A.*, 2016, **113**, 14201–14206.
26 P. C. Wu, W.-Y. Tsai, W. T. Chen, Y.-W. Huang, T.-Y. Chen, J.-W. Chen, C. Y. Liao, C. H. Chu, G. Sun and D. P. Tsai, *Nano Lett.*, 2017, **17**, 445–452.
27 X. Zhu, G. M. Imran Hossain, M. George, A. Farhang, A. Cicek and A. A. Yanik, *ACS Photonics*, 2020, **7**, 416–424.
28 B. Lamprecht, G. Schider, R. Lechner, H. Ditlbacher, J. R. Krenn, A. Leitner and F. R. Aussenegg, *Phys. Rev. Lett.*, 2000, **84**, 4721.
29 N. Félidj, G. Laurent, J. Aubard, G. Lévi, A. Hohenau, J. Krenn and F. Aussenegg, *J. Chem. Phys.*, 2005, **123**, 045430.
30 T. Teperik and A. Degiron, *Phys. Rev. B: Condens. Matter Mater. Phys.*, 2012, **86**, 245425.
31 C. Cherqui, M. R. Bourgeois, D. Wang and G. C. Schatz, *Acc. Chem. Res.*, 2019, **52**, 2548–2558.
32 R. Guo, T. K. Hakala and P. Törmä, *Phys. Rev. B*, 2017, **95**, 155423.
33 V. G. Kravets, A. V. Kabashin, W. L. Barnes and A. N. Grigorenko, *Chem. Rev.*, 2018, **118**, 5912–5951.
34 V. Tretnak, U. Hohenester, J. R. Krenn and A. Hohenau, *J. Phys. Chem. C*, 2019, **124**, 2104–2112.
35 M. Braïk, T. Geronimi-Jourdain, S. Lau-Truong, A. Belkhir, S. Gam-Derouich, A. Chevillot-Biraud, C. Mangeney and N. Félidj, *Nanophotonics*, 2023, **12**, 2179–2188.
36 D. Dey and G. C. Schatz, *MRS Bull.*, 2024, **49**, 421–430.
37 L. Dehbi, P. Kartikey, M. Braik, A. Belkhir, S. Lau-Truong, S. Gam-Derouich, A. Chevillot-Biraud, C. Mangeney, A. Mezeghrane, F. I. Baida and F. Nordin, *Nanoscale*, 2025, 1536–1543.
38 A. Danilov, G. Tselikov, F. Wu, V. G. Kravets, I. Ozerov, F. Bedu, A. N. Grigorenko and A. V. Kabashin, *Biosens. Bioelectron.*, 2018, **104**, 102–112.
39 A. D. Humphrey and W. L. Barnes, *Phys. Rev. B: Condens. Matter Mater. Phys.*, 2014, **90**, 075404.
40 I. Ragheb, M. Braik, A. Mezeghrane, L. Boubekeur-Lecaque, A. Belkhir and N. Felidj, *J. Opt. Soc. Am. B*, 2019, **36**, E36–E41.
41 B.-W. Lin, Z. Wang, Y.-L. Ho, Y.-C. Lee, D. Xing, Y.-T. Lee and J.-J. Delaunay, *Appl. Phys. Lett.*, 2024, **124**, 211701.
42 O. Lecarme, Q. Sun, K. Ueno and H. Misawa, *ACS Photonics*, 2014, **1**, 538–546.
43 T. Pakizeh, *J. Phys. Chem. C*, 2011, **115**, 21826–21831.
44 T. Simon, X. Li, J. Martin, D. Khlopin, O. Stéphan, M. Kociak and D. Gérard, *Proc. Natl. Acad. Sci. U. S. A.*, 2022, **119**, e2116833119.
45 L. Li and W. Wu, *Appl. Phys. Lett.*, 2024, **124**, 071701.
46 L. Li, Y. Ouyang, L. Ma, H. Sun, Y. Chen, M. Wu, Z. Qi and W. Wu, *Photonics Res.*, 2023, **11**, 2210–2221.
47 M. Saad Bin-Alam, O. Reshef, R. Naeem Ahmad, J. Upham, M. J. Huttunen, K. Dolgaleva and R. W. Boyd, *Opt. Lett.*, 2022, **47**, 2105–2108.
48 D. Men, H. Wang, Q. Ding, Y. Wu, T. Wu, W. Qu, L. Ma, H. Zhang, G. Jiang and L. Hang, *J. Mater. Chem. C*, 2024, **12**, 3254–3260.
49 X. Yang, D. Xia and J. Li, *Nanotechnology*, 2022, **33**, 445201.
50 M. J. Tan, J.-E. Park, F. Freire-Fernández, J. Guan, X. G. Juarez and T. W. Odom, *Adv. Mater.*, 2022, **34**, 2203999.
51 Y. Conti, N. Passarelli, J. Mendoza-Carreño, L. Scarabelli and A. Mihi, *Adv. Opt. Mater.*, 2023, **11**, 2300983.
52 Y. Conti, X. He, Y.-C. Chen, N. Chiang and L. Scarabelli, *Adv. Photonics Res.*, 2025, 2500075.
53 Y. Conti, N. Chiang and L. Scarabelli, *ChemNanoMat*, 2024, **10**, e202300566.
54 A. D. Rakić, *Appl. Opt.*, 1995, **34**, 4755–4767.
55 D. Khlopin, F. Laux, W. P. Wardley, J. Martin, G. A. Wurtz, J. Plain, N. Bonod, A. V. Zayats, W. Dickson and D. Gérard, *J. Opt. Soc. Am. B*, 2017, **34**, 691–700.
56 A. Minenkov, S. Hollweger, J. Duchoslav, O. Erdene-Ochir, M. Weise, E. Ermilova, A. Hertwig and M. Schiek, *ACS Appl. Mater. Interfaces*, 2024, **16**, 9517–9531.
57 S. D'Elia, N. Scaramuzza, F. Ciuchi, C. Versace, G. Strangi and R. Bartolino, *Appl. Surf. Sci.*, 2009, **255**, 7203–7211.
58 N. M. Ahmed, F. A. Sabah, H. Abdulgafour, A. Alsadig, A. Sulieman and M. Alkhoaryef, *Results Phys.*, 2019, **13**, 102159.
59 R. Guo, L. Chen, Z. Yan, R. Ma, S. Feng and S. Deng, *J. Phys. Chem. C*, 2024, **128**, 11298–11305.
60 A. Movsesyan, A. Muravitskaya, M. Castilla, S. Kostcheev, J. Proust, J. Plain, A.-L. Baudrion, R. Vincent and P.-M. Adam, *J. Phys. Chem. C*, 2020, **125**, 724–731.
61 I. Zorić, M. Zäch, B. Kasemo and C. Langhammer, *ACS Nano*, 2011, **5**, 2535–2546.
62 W. Gotschy, K. Vonmetz, A. Leitner and F. Aussenegg, *Appl. Phys. B:Lasers Opt.*, 1996, **63**, 381–384.
63 A. Hohenau, H. Ditlbacher, B. Lamprecht, J. R. Krenn, A. Leitner and F. R. Aussenegg, *Microelectron. Eng.*, 2006, **83**, 1464–1467.